Electrochemical CO_2 reduction in ionic liquids: a 3D modeling approach

Journal of Physics: Energy

PAPER

Electrochemical CO_2 reduction in ionic liquids: a 3D modeling approach

Inês S Fernandes[1], **Sofia Messias**[1,2], **Rodrigo Martins**[1], **Manuel J Mendes**[1,*] **and Ana S Reis-Machado**[1,2,*]

[1] i3N/CENIMAT, Department of Materials Science, NOVA School of Science and Technology and CEMOP/UNINOVA, Campus de Caparica, 2829-516 Caparica, Portugal
[2] LAQV, REQUIMTE, Department of Chemistry, NOVA School of Science and Technology, 2829-516 Caparica, Portugal
* Authors to whom any correspondence should be addressed.

E-mail: mj.mendes@fct.unl.pt and ams.machado@fct.unl.pt

OPEN ACCESS

RECEIVED
14 April 2025

REVISED
22 July 2025

ACCEPTED FOR PUBLICATION
1 August 2025

PUBLISHED
14 August 2025

Keywords: sustainable carbon-to-fuel conversion, electrochemical CO_2 reduction, 3D finite-elements modeling, porous cathodes, ionic liquid-based electrolytes

Supplementary material for this article is available online

Abstract

The escalating pressure to mitigate CO_2 emissions calls for novel approaches to produce sustainable fuels and chemicals, as means to close the anthropogenic cycle. This study fulfills a critical need in this field, through the development of modeling tools capable of guiding groundbreaking technical advances in liquid-phase electrochemical CO_2 reduction (ECR). An unprecedented 3D model for porous cathodes was designed for the co-electrolysis of CO_2 and water to produce syngas, particularly considering aqueous and ionic liquid (IL) electrolytes to increase CO_2 solubility in the electrolyte while lowering its density and kinematic viscosity to boost ECR process performance. The structural parameters of the cathode, i.e. porosity and pores geometry, were investigated, together with the effects of operational parameters such as type of electrolyte, flow rate, temperature and pressure. A key outcome was the demonstration of a flow electrolytic system, coupled with an improved porous zinc cathode, capable of producing CO partial current densities of 231 mA cm^{-2} at −1.1 V vs. RHE, with a composition suitable for up-stream methane production (H_2:CO ratio of 3:1), at 10 bar, 45 °C, and 10 mL min^{-1}, reaching the threshold for industrial-relevant yields. Such results show that the combination of tailored IL-based electrolytes and advanced cathode design enables to greatly overcome mass transport limitations and improve reaction dynamics. These results open a new path towards the use of computational smart-search methods to improve the industrial implementation of ECR in liquid-phase.

1. Introduction

Electrochemical CO_2 reduction (ECR) belongs to the group of carbon capture and utilization (CCU) technologies in which CO_2 is converted into green fuels and chemicals that can be used as building blocks for various industries. The significance of CCU for a sustainable economy has been highlighted by many studies, as that of Mertens *et al* [1], while ECR at high pressure is addressed by Reis-Machado and Nunes da Ponte [2]. The R&D challenges associated with such topics have been fostering a broad range of materials-related research. For instance, Chang *et al* [3] reviewed copper-based catalysts for ECR to multi-carbon products. Messias *et al* [4] presented an overview of carbon materials as cathode constituents for ECR. Habibzadeh *et al* [5] discussed different types of membranes used in electrolyzers for ECR, and Yang and Yi [6] analyzed different reactor designs for ECR.

The ECR process involves the use of an electrochemical cell which can be powered by renewable energy sources to electrically drive the reduction of CO_2 and water at the cathode, thereby allowing the creation of carbon-neutral energy-supply cycles; for instance for renewable methane production (e.g. solar methane) [7] which is promising for buildings application [8]. An example of an ECR system, where CO_2 is fed dissolved in the liquid electrolyte, is illustrated in figure 1(a) and, a system where CO_2 is fed in the gaseous-phase is

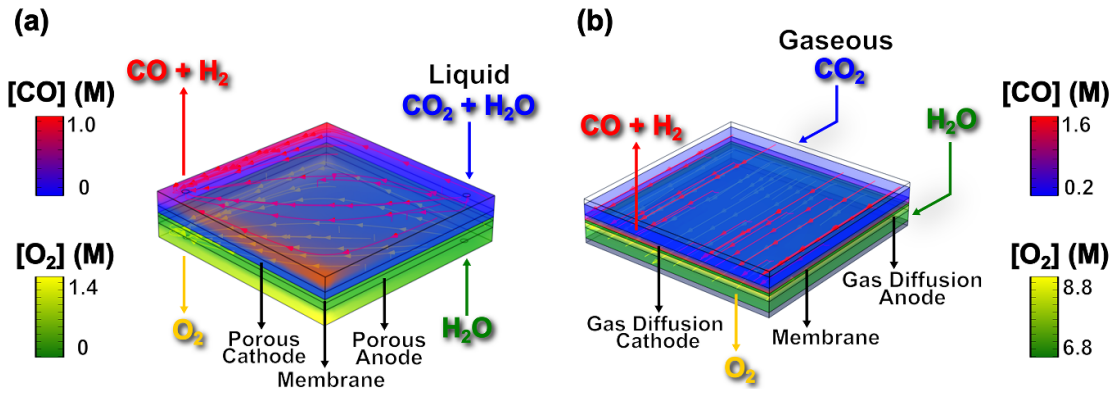

Figure 1. CO_2 and H_2O co-electrolysis in membrane-electrode assembly (MEA) electrolyzers in (a) liquid-phase, and (b) gas-phase. The colored bars show oxygen molar concentration in mol L^{-1} (M), carbon monoxide molar concentration in mol L^{-1} (M).

depicted in figure 1(b). Additionally, the systems display the flow streams of the particular relative positioning of the inlets and outlets addressed in this work. In figure 1(a), these features are located on the lateral side of the cell, with the liquid inflows on the bottom and the gaseous outflows on the top. In contrast, the configuration in figure 1(b) shows only gaseous-phase inflows and outflows, the first ones being normal-aligned to the bottom plane, while the second ones have the same alignment but regarding the top planes of the electrolytic cell.

The present work addresses the production of syngas, a mixture of carbon monoxide and hydrogen. In acidic medium, the anodic reaction is given by equation (1) and the cathodic reactions are given by equations (2) and (3),

Anode reaction:

$$2\,H_2O\,(l) \leftrightarrow O_2\,(g) + 4\,H^+\,(aq) + 4e^-. \tag{1}$$

Cathode reactions:

$$2\,H^+\,(aq) + 2\,e^- \leftrightarrow H_2\,(g) \tag{2}$$

$$CO_2\,(aq) + 2\,H^+\,(aq) + 2e^- \rightarrow CO\,(g) + H_2O\,(l)\,. \tag{3}$$

There are many critical parameters that influence the performance of ECR, such as the nature of the catalysts, electrolyte type, electrolyzer design, operation conditions, etc. As such, computational modeling tools can be extremely useful to aid experimental development work.

The poor solubility of CO_2 in water (33 mM at 25 °C and atmospheric pressure) has motivated several studies to model gas diffusion electrodes (GDEs) used in gas-phase ECR. In this technology, CO_2 is directly fed in the form of gas to the GDEs, reducing diffusion limitations that occur in liquid systems, increasing the availability for reaction at catalyst surfaces and leading to a substantial decrease in overpotentials, especially at high current densities. Delacourt *et al* [9] derived a general framework for treating equilibrated reactions and interfacial mass transfer in a multiphase medium for implementation in an electrolysis cell model. Georgopoulou *et al* [10] developed a model for CO_2 conversion into formate/formic acid by combining individual analytical sub-models of the different mechanisms involved in the physical process. Dinh *et al* [11] used density functional theory to assess the impact of hydroxide ions on the thermodynamic and activation energy barriers of the CO dimerization step, showing that the presence of hydroxide lowers the binding energy of CO on the Cu surface. Besides, these authors also elaborated a reaction diffusion model which showed that the reaction takes place near an abrupt interface, improving reaction kinetics for CO dimerization into ethylene. Tan *et al* [12] modeled local CO_2 concentration to promote C-C coupling. Weng *et al* [13] reported the development and application of a multiphysics model to investigate membrane electrode assemblies to guide the design of ECR cells. Breé *et al* [14] compared different reactors for CO_2 reduction by developing modular mechanistic dynamic models to improve performance. El-Shafie *et al* [15] investigated the role of Cu_2O-ZnO based GDEs in enhancing the reduction of CO_2 into methanol. Wheeler *et al* [16] developed a 3D model using COMSOL Multiphysics to investigate the molar fraction of water at the cathodic GDE/membrane interface, While Kas *et al* [17] developed another multiphysics model to

examine the impact of the gradient on the spacioactivity of GDES at high current density. Blake *et al* [18] derived an analytical approximation of cathodic layer dynamics, and used it to determine the effect of carbonate on cell performance and how the state of the equilibrium reactions can be influenced by the cell parameters. Heßelmann *et al* [19] reported a one-dimensional steady state model of the GDE to investigate the influence of relevant operational parameters and GDE properties on CO_2 reduction. All in all, it has become clear that GDEs can significantly enhance CO_2 reduction performance by increasing mass transport. They show increased kinetic rates and Faradaic efficiencies (FEs %) compared to planar foil electrodes [20]. Multiphysics models have been developed to investigate the interplay between reagents transport and reaction kinetics in GDEs, which have nonetheless revealed that GDE performance continues to be limited by CO_2 mass transport at high current densities [21]. The primary drivers for such transport limitations at high current densities are flooding, due to water crossover from anode to cathode, and salt precipitation due to accumulation of K_2CO_3 or other salts in the cathode.

It is also noticed that carbon delivery efficiency decreases due to chemical absorption of CO_2 in the electrolyte [22]. Microfluidic CO_2 electrolyzers promise to achieve improved mass transfer properties and higher CO partial current density by using anisotropic layers and electrodes with optimized porosity [23].

Since the 1980's, liquid-phase electrolyzers have become a common setup for studying ECR in aqueous solutions. Examples of such studies are: the seminal work of Hori *et al* [24] examined the production of methane and ethylene at copper electrodes, the enhanced formation of ethylene and alcohols [25], the reduction into CO [26], and the study of CO_2 reduction at copper single crystals [27]. For that, the use of porous cathodes with substantial increased surface areas has been another subject of much investigation. Kas *et al* [28] prepared a Cu hollow fiber as gas diffuser obtaining high CO production rates comparable to those achieved by the use of noble metals catalysts. However, it was observed in a highly porous Cu catalyst that the formation of carbonate salt still blocked the pores of the catalysts and the gas diffusion layer, giving rise to voltage losses and species transport issues at the interface [29]. The improved catalytic performance, due to the use of porous electrodes was also ascribed to the hindrance of proton mass transport within the porous network inhibiting the hydrogen evolution reaction [30]. However, these systems face a major challenge: low CO_2 solubility in water, which limits how much CO_2 reaches the depth of the porous channels of the cathodes. Even with technologies like flow cells to improve the reagents diffusion, issues like limited mass transfer and low reaction rates persist [31]. Yang *et al* [32] prepared atomically dispersed nickel on nitrogenated graphene and converted CO_2 into CO, with a maximum CO FE_{CO} of 97% and partial current density of 22 mA cm^{-2} at 0.72 V versus RHE in $KHCO_3$ electrolyte. This work illustrates the highest ranges of current densities obtained when aqueous electrolytes are used in H-cells. Asadi *et al* [33] employing MoS_2 catalyst obtained one of the highest reported current densities, 65 mA cm^{-2} in converting CO_2 into CO in an ionic liquid (IL)-based electrolyte at −0.76 V versus RHE with an FE of ca. 98%. Nevertheless, current densities often limited to about 60 mA cm^{-2} [34] are far below the 200 mA cm^{-2} needed for commercial viability together with ca. 70% FE for the desired product, overpotentials below 1.0 V, and operation times over 8000 h or one year [35].

It is known that CO_2 solubility increases with pressure in aqueous media [36], but this does not necessarily result in higher current densities. The depth of penetration of the CO_2 into the channels of the porous cathode has strong diffusion boundaries (just some microns) [37] and often low selectivity limits the economic viability of the overall process. Thus, ECR in liquid-phase is still at a low maturity stage. This work aims at advancing the maturity of ECR in liquid phase by exploiting the potential of flexibility, robustness and stability of this technology.

Room temperature ILs are salts that are liquid at temperatures below 100 °C. Some families of ILs are good solvents for CO_2. Besides, some of these ILs exhibit negligible volatility and excellent chemical and electrochemical solubilities demonstrating many interesting advantages for the ECR compared to purely aqueous electrolytes. One of these advantages is the increased CO_2 solubility allowing enhancing CO_2 availability at the electrode surface for reaction, leading to improved current densities. In one of the pioneering works of ECR with ILs, Rosen *et al* [38] reported an electrocatalytic system that reduces CO_2 to CO at applied potential of 1.5 V, almost at the equilibrium potential (1.33 V), with a liquid-phase electrolyzer using IL. This electrolyte decreases the initial reduction energy barrier by complexation of the formation energy of the anion radical CO_2intermediate. ILs are generally more viscous than water. However, the addition of water decreases the viscosity of the IL-based electrolytes while simultaneously serving as a proton source. Depending on the nature of IL it was shown that there is the potential of finding aqueous IL-based electrolytes that have the advantages of both aqueous electrolytes and IL electrolytes, such as green nature, increased productivities, selectivities and lower costs (Messias *et al* [39]).

The Fernandes *et al* [40] have developed a two-dimensional finite-elements model for porous zinc cathodes to improve the performance of ECR in aqueous electrolytes using optimization algorithms to enhance structural and operational parameters, and thus achieve higher current densities. In this paper, an

experimentally validated 2D computational model of porous zinc cathodes shows great potential for advancing CO_2 electroreduction technology in liquid phase. The production of CO from CO_2 electroreduction can be increased by applying recommendations from the developed model, through smart-search optimization algorithms, and parametric sweep studies of fluid dynamics variables. The model revealed conditions that allowed a significant 486% enhancement in current density compared to experimental results, by enhancing cathode porosity, number of cathodic fibers, fiber geometrical shape, catholyte flow rate, temperature, and pressure.

The present work consists of a crucial step forward by developing a 3D cathode design much closer to physical reality, accounting for added volume-related factors such as the cathode thickness. The increase in complexity consequently raises the time of the simulation runs, as the number of degrees of freedom, and hence the number of finite-elements for the method convergence increases exponentially. The results obtained are compared with those of the 2D model [40] and the impact of the use of the aqueous IL 1-ethyl-3-methyl-imidazolium trifluoromethanesulfonate (triflate)—[EMIM][OTf] is investigated. To our best knowledge, this is an unprecedented 3D numerical simulation study involving an aqueous IL-based electrolyte for ECR.

2. Methodology

The COMSOL Multiphysics® version 6.1 (COMSOL AB, Stockholm, Sweden) software was employed in this work, given its pivotal capability in providing better understanding of the mechanisms involved in the dynamics of complex systems, by integrating different physical/chemical processes. It also has a user-friendly interface, which allows the development of complex design models for reliable simulations and smart-search optimizations.

This software was employed to improve the design of porous cathodes for ECR processes. The 3D design of cathodes was developed, which in turn made it possible to simulate the electrochemical reactions at the electrode/electrolyte interface. By focusing on optimizing the porous cathodes through the fine-tuning of several model parameters, it was possible to largely enhance the performance of the electrolytic process to produce syngas with maximized rates to be used in methane synthesis.

Besides the geometrical properties of the porous cathode, other modules provided by COMSOL Multiphysics®, such as laminar flow, secondary current distribution and transport of diluted species, were employed to attain a better understanding of the overall operation performance.

One of the strengths of this methodology is its adaptability, as it allows to conduct simulations of electrochemical systems under a wide range of scenarios. The model was created in a versatile form that makes it applicable for any set of electro-conductive materials used for the components of the electrochemical cell, despite their diversified physical properties. This model was validated and tested in this work with zinc-based porous cathodes, but many other electrode materials and geometries can be simulated.

Stability studies are forecasted for the developed porous cathodes according to simulation guidelines, and preliminary studies of the stability of zinc porous cathodes can be found in Luo *et al* [41].

Concerning the electrolyte, to undertake a comparative analysis of the benefits of using an aqueous IL-based electrolyte vs. a purely aqueous electrolyte, with the same 3D design as the porous cathode, four different models were created and validated with experimental data. Namely, two models were developed for the description of batch operations using IL-based (Model A) and aqueous (Model B) electrolytes. Other two models were tested and employed for the continuous flow operations, one for the IL case (Model C) and another for the aqueous medium (Model D). This information is systemized in table 1, along with the main process performance values, such as CO and syngas (H_2+CO) FE (FE_{CO}, FE_{syngas}, %), as well as energy efficiency (EE, %).

The authors note that the main goal of the present study is to obtain guidance from the constructed models to maximize the CO partial current density produced by the porous cathodes at a specific applied potential, in view of up-stream methane synthesis. As such, the models A and C employed in this work for the IL-based electrolyte targeted a syngas composition suitable for methane synthesis (H_2:CO ratio of 3:1), corresponding to FE_{CO} of 25% and FE_{syngas} of 80% (equation supplementary material (SM.1)). On the other hand, the aqueous models B and D serve mostly for a comparative analysis with previous simulation results [41], which did not target such H_2:CO ratio for methane, yielding a higher FE_{CO} of 80% and FE_{syngas} of 95%. Besides, Models B and D also illustrate the impact of the use of IL in the electrolyte composition. The differences in electrical-to-fuel EE between these cases are due to the fact that producing only CO is less energy-demanding (EE = 44%, given by equation SM.2) than synthesizing the two products—H_2 and CO (EE = 35%, given by equation SM.3).

Table 1. Characteristics of the four 3D models developed in this work, and experimentally corroborated, listing operation regime, electrolyte type, CO and syngas Faradaic efficiencies (FE_{CO}, FE_{syngas}, %), as well as total energy efficiency (EE %), at the applied potential of −1.1 V vs. RHE.

Designation	Regime	Electrolyte type	FE_{CO} (%)	FE_{syngas} (%)	Total EE (%)
Model A	Batch	IL: 10% wt. [EMIM][OTf]	25	80	35
Model B	Batch	Aqueous: 0.1 M $KHCO_3$	80[a]	95[a]	44[a]
Model C	Continuous flow	IL: 10% wt. [EMIM][OTf]	25	80	35
Model D	Continuous flow	Aqueous: 0.1 M $KHCO_3$	80[a]	95[a]	44[a]

[a] Values estimated from Luo *et al* [41].

2.1. Experimental procedure for validation

2.1.1. Materials and reagents

Carbon dioxide (N45, purity 99.995%) was purchased from Air liquide. 1-ethyl-3-methylimidazolium trifluoromethanesulfonate (triflate) >99% purity was purchased from Iolitec and dried overnight before use. Commercial zinc foils were purchased from Francisco Soares Lda.

2.1.2. Electrochemical measurements

Electrolyses were carried out in a high pressure two compartment electrochemical cell designed and constructed in our laboratory. This cell is described in detail elsewhere [42]. It consists of a two-electrode system. The working electrode used was a commercial zinc foil and the anode was a commercial IrO_2/Ti mesh purchased from DeNora. The dimensions of the electrodes were 6 cm × 6 cm × 0.1 cm.

After assembling the electrochemical reactor, the electrolyte was pumped into the reactor. CO_2 was then introduced into the facility. Teledyne Isco syringe pumps, model 500D, were used for charging the electrolyte. Then, carbon dioxide was brought to the desired pressure, and when the reactor stabilized at the desired temperature and pressure, current was applied to the electrodes and electrolysis was initiated. Different currents were applied and the potential measured to obtain the polarization curve. A potentiostat/galvanostat (PGSTAT128N-Autolab 84469) was used. Electrolyses were carried out in batch mode.

After the electrolysis, a sample of the gaseous mixture produced is analyzed using gas chromatography (GC). The gas chromatograph used is an Agilent Micro GC 3000, which is equipped with a thermal conductivity detector and two columns (a molecular sieve and a Plot U column) to separate and analyze the gases. Gases as H_2, N_2, O_2, CO, and CH_4 are analyzed using the molecular sieve column, while CO_2 and higher hydrocarbons are quantified with the Plot U column. The composition of the gaseous mixture is determined by comparing the measured results with calibrated mixtures of known compositions.

2.2. Geometry of the models

Figure 2 illustrates the cathodes geometrical models. In the previous 2D model developed by the present authors [40], shown in figures 2(a) and (c), the actual pore diameter served only as an indicator of the distance between fibers (d_p, μm), n is the number of fibers, and the fiber length was calculated based on the side length of the cathode (L, μm) considered for spatial modeling boundaries ($L = 975$ μm in the case of the present study).

At first glance the 2D structure gave the erroneous visual impression that the fibers were, in fact, pores. To simulate a continuous creeping flow system (characteristic of porous structures) from inlet to outlet, and free from coalescence effects, the solid fiber surfaces forming the cathode could not touch each other under any conditions, regardless of porosity, number of fibers, or fiber geometry. Furthermore, the flow direction was perpendicular to the cathode fibers. This design deviates significantly from the real porous cathodes. To improve cathode description a 3D model design was created. A detailed schematic of this structure can be consulted in figure SM.1 for better understanding of the model geometry. In this model the electrolyte flows through the cathode pores as illustrated in figures 2(b) and (d). There are four main variables to consider: the cathode side length L (μm), the number of pores per side n_L, the cathode porosity ε, and the cathode thickness D (mm). These dimensions are shown in figures 2(b) and (d).

Given these four dimensions, a set of other variables to describe this system can be deduced, such as: pore diameter d_p (μm), fiber length d_f (μm), total number of pores n, and superficial pore area S (m^2), and electrode volume V (m^3), given respectively by equations (4)–(8),

$$d_p = \sqrt{\frac{\varepsilon}{\frac{\pi}{4}\frac{n}{L^2}}} \tag{4}$$

$$d_f = \frac{L}{n_L} - d_p \tag{5}$$

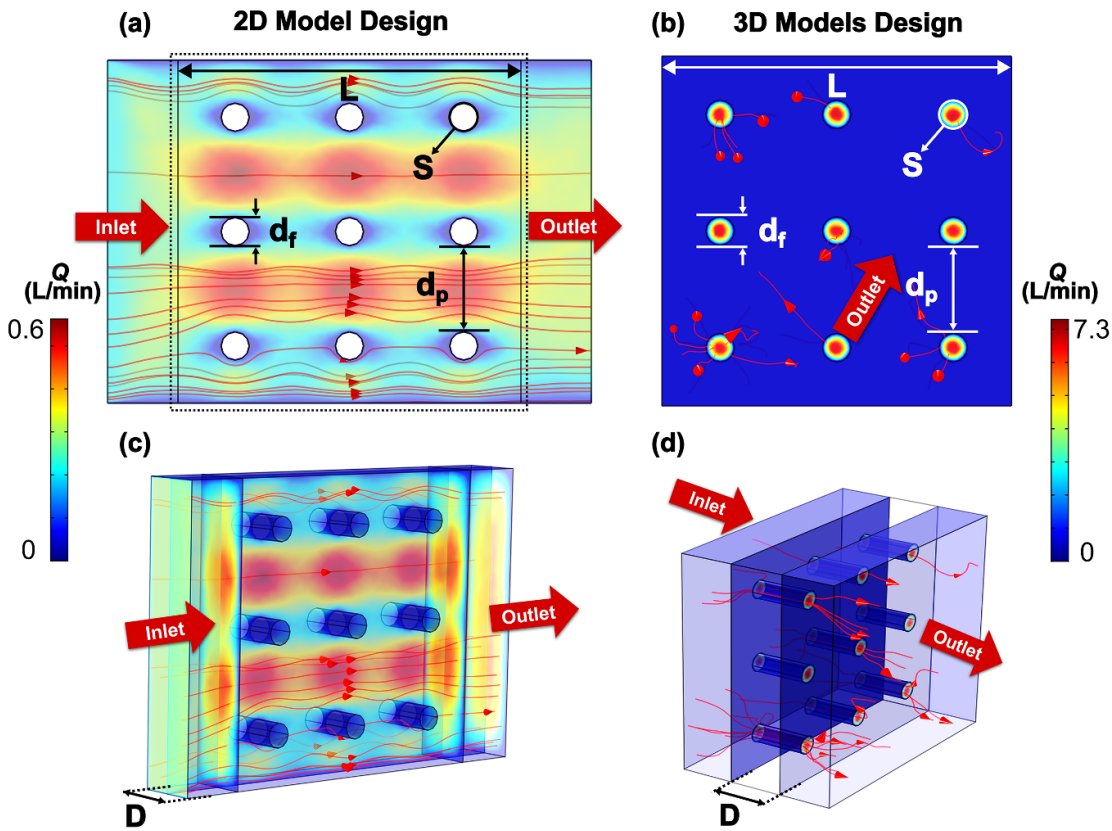

Figure 2. Comparison between the 2D/3D geometrical and operational designs of the ECR models from (a), (c) the previous modeling article by S. Fernandes et al, and (b), (d) the present study. Cathode side (L, mm), cathode thickness (D, mm), electrolyte flow rate (colored bars, Q, mL min^{-1}), (a), (c) pore length (d_p, μm), fiber diameter (d_f, μm), fiber surface area (S, m), (b), (d) pore diameter (d_p, mm), fiber length (d_f, mm), pore surface area (S, m). (a), (c) adapted with permission from [40]. CC BY-NC-ND 4.0.

$$n = n_L^2 \tag{6}$$

$$S = Dd_p \pi n \tag{7}$$

$$V = DL^2(1-\varepsilon). \tag{8}$$

To clearly outline the geometric, structural, and operational differences between the 2D and 3D models created, table 2 summarizes the main differences of both types of models. The list of symbols and abbreviations can be found in SMs.

In the newly refined design of the 3D ECR models proposed here, no geometric or structural approximations were applied relative to the experimental porous cathodes used for theoretical validation, apart from the downscaling of the modeled area. This downscale focused on approximately 1.0 mm^2 of the total 36 cm^2 geometric surface area of the porous cathodes.

2.3. Assumptions of the 3D models

These models incorporate fluid dynamics, transport processes of (diluted) chemical species, and electrochemical processes performed in an aqueous medium, which creates a very complex system that is described mathematically with non-linear and partial differential equations.

This model takes into consideration convection, migration and diffusion of the charged species which control the performance of porous cathodes.

In essence, i.e., to facilitate implementation of the numerical mesh software, some physical approximations were made to the transport of diluted charged species:

1) The cathodic fibers were taken to be isotropic and homogenous.
2) It was postulated that the electrolyte accommodates no turbulence, and therefore, it approximates to a laminar flow.
3) It was assumed that the fluid is incompressible, isothermal and diluted in nature.
4) There was no gravitational field effect considered.
5) The ECR process operates in stationary-state mode, hence, all time-dependent influences are disregarded.

Table 2. Comparison between geometry design and boundary conditions of the 2D model from Fernandes *et al* [40], and the four proposed 3D models from the present article.

Features	3D model design	2D model design
Study type	Steady state	Steady state
Flow regime	Laminar flow	Creeping flow
Species transport	Diluted species	Diluted species
Current distribution	Secondary	Secondary
Inlet	Normal to CSP, bottom	Parallel to CSP, left
Outlet	Normal to CSP, top	Parallel to CSP, right
Depth	$D = 1.25/2.00$ mm (z-axis)	No z-axis
Length	$L = 975$ μm (xy-plane)	$L = 975$ μm (xy-plane)
Liquid space	Pore diameter (d_p, μm)	Pore length (d_p, μm)
Solid space	Fiber length (d_f, μm)	Fiber diameter (d_f, μm)
Surface area	$S = Dd_p\pi\, n$ (m^2)	$S = d_f\pi\, n$ (m)
Solid volume	$V = DL^2\,(1-\varepsilon)$ (m^3)	$V = L^2\,(1-\varepsilon)$ (m^2)
Volumetric area	$A_v = S/V$ (m^{-1}, same value)	$A_v = S/V$ (m^{-1}, same value)
Pressure constraints	Inlet + Outlet (P, bar)	Inlet (P_{in}, bar)
Flow rate constraints	Inlet + Outlet (Q, bar)	Outlet (Q_{out}, mL min^{-1})
Concentration constraints	Inlet ($c_{i,0}$, M)	Inlet ($c_{i,0}$, M)

Cathode surface plane (CSP), inlet pressure (P_{in}, bar), and outflow rate (Q_{out}, mL min^{-1}), initial concentration of species i at inlet ($c_{i,0}$, M), cathode volumetric area (A_V, m^{-1}).

6) For electro-reduction of CO_2 into CO, a first-order kinetic reaction was considered.
7) The simulation work was undertaken for constant values of FE_{CO}, FE_{syngas} and total EE for each applied potential in the voltage range of the polarization curves (used for experimental validation of the developed models).

2.4. Development of multiphysics models

2.4.1. Fluid dynamics

The fluid flow is described as a 3D laminar flow regime and the pressure drop is given by the Navier–Stokes equations, equations (9) and (10), where the fluid surface velocity vector is u (m s^{-1}), the electrolyte density is ρ (kg m^{-3}), the pressure is p (Pa), and the dynamic fluid viscosity is ν(m^2 s^{-1}),

$$\nabla u = 0 \tag{9}$$

$$(u\nabla)\,u + \frac{1}{\rho}\nabla p - \nu\nabla^2 u = 0. \tag{10}$$

Since the Reynolds number (Re, calculated by equation SM.5) is below five in all the studied cases, the flow can be classified as laminar. According to established porous media flow theory, the flow remains within the laminar regime for Reynolds numbers below approximately 10, with Darcy's law applicable in the strictly viscous range (Re < 1) and inertial corrections becoming relevant as Re approaches 10. Therefore, the use of laminar flow assumptions is justified in these cases, as can be observed in figure SM.2, and quantitively confirmed in table SM.2 [43].

2.4.2. Diluted species transport

The conservation equation of species and electrical charges of the electrolyte utilized in this model is given by equation (11). The concentration of species i is c_i (mol m^{-3}), the electric charge number of species i is z_i, the diffusion coefficient of species i is D_i (m^2 s^{-1}), the (total) electric potential is Φ (V vs. RHE), the molar gas constant is $R = 8.3145$ J (mol·K)$^{-1}$, and the temperature is T (K),

$$D_i\nabla^2 c_i - \nabla\left(\frac{D_i z_i c_i}{RT}\right)\nabla\phi + u\nabla c_i. \tag{11}$$

2.4.3. Electrochemistry

The electrical neutrality of the electrolyte was described by equation (12),

$$\sum_i z_i c_i = 0. \tag{12}$$

The conservation balance of charge is considered according to equation (13). The total current density is i (A m^{-2}), while i_l (A m^{-2}) is the current density of the electrolyte and i_s (A m^{-2}) is the current density of

the electrode,

$$\nabla i_l = -\nabla i_s = \nabla i. \tag{13}$$

The current density of the electrolyte is given by equation (14). Faraday's constant is $F = 9.6485 \times 10^4$ C mol^{-1}, the electric potential and conductivity of the electrolyte are Φ_l (V vs. RHE) and σ_l (S m^{-1}), respectively,

$$i_l = F\sum_{i=1}^{n} z_i\left(-D_i - \sigma_l \nabla \phi_l\right). \tag{14}$$

The Ohm's law was applied to the electric potentials in order to calculate the currents as in equation (15). The current density of the electrode is i_s (A m^{-2}), the electric potential and conductivity of the electrode are Φ_s (V vs. RHE) and σ_s (S m^{-1}), respectively,

$$i_{l/s} = -\sigma_{l/s} \nabla \phi_{l/s}. \tag{15}$$

The Nernst equation was used on the porous cathode surface to determine the equilibrium potential of the governing electrochemical reaction, as given by equation (16). The chemical activity of the reduced and oxidized species is a_{R} and a_{O}, respectively. They are equal to the ratio between local (c_i, mol m^{-3}) and initial ($c_{i,0}$, mol m^{-3}) concentrations of each of these types of species. The ECR equilibrium potential is E_{eq} (V vs. RHE), its reference equilibrium potential is $E_{\mathrm{eq,ref}}$ (V vs. RHE), and the number of electrons transferred in the reaction is n_{e}.

$$E_{\mathrm{eq}} = E_{\mathrm{eq,ref}} - \frac{RT}{n_{\mathrm{e}}F} \ln\left(\frac{a_{\mathrm{R}}}{a_{\mathrm{O}}}\right). \tag{16}$$

The total current density (cathodic and anodic) was calculated by the Butler–Volmer equation, equation (17), which was used to define the electrochemical reaction (ECR) that happens on the surface of the porous cathode. The ECR cathodic transfer coefficient is α_{c}, while its anodic transfer coefficient is α_{a} and the overpotential is η (V vs. RHE), defined by Eq. SM.4. The variable $i_{\mathrm{o,ref,IL/aq}}$ (A cm^{-2}) stands for the ECR-to-CO reference exchange current density inside purely aqueous (aq), or IL-based (IL) electrolytes,

$$i = i_{\mathrm{o,ref,IL/aq}}\left[a_{\mathrm{R}} \exp\left(\frac{\alpha_{\mathrm{a}} neF\eta}{RT}\right) - a_{\mathrm{O}} exp\left(\frac{-\alpha_{\mathrm{c}} neF\eta}{RT}\right)\right]. \tag{17}$$

For implementation of all the previously mentioned equations on the modeling software, the electrochemical constants and the operational parameters used in this work simulations are presented below in table 3.

2.4.4. Boundary conditions

As mentioned earlier, this model was assumed to work in steady state operation.

The top and bottom cathode geometric design boundaries had null species transport flow, as was defined by equation (18). The species transport molar flow is N_i (mol s^{-1}), the outward normal unit vector is $\vec{n}$ (m s^{-1}),

$$N_i \vec{n} = 0 \begin{cases} 0 \leqslant x \leqslant L, y = 0 \\ 0 \leqslant x \leqslant L, y = L \end{cases} \tag{18}$$

The following Neumann condition, equation (19), responsible for regulating the pressure of the porous cathode, was applied to all limits of the integration domains of the model, except for the inlet and outlet boundaries:

$$\nabla p\vec{n} = 0. \tag{19}$$

The inlet boundary was defined to be constrained by the entry of the species with its initial concentration in the electrolyte solution, as stated by equation (20),

$$c_i = c_{i,0}. \tag{20}$$

The outlet boundary was defined by equation (21) according to the outward normal unit vector of the species concentration from the cathodic compartment,

$$-\vec{n} D_i \nabla c_i = 0. \tag{21}$$

Table 3. ECR species transport and electrochemistry parameters.

Designation	Symbol	Value	Units	References
Electrode conductivity	σ_s	16.6×10^6	S m^{-1}	[44]
Reference equilibrium potential at pH = 0 (vs. RHE)	$E_{eq,ref}$	−0.10	V	[45]
Kinetic rate constant in IL-based electrolyte	$k_{CO2,IL}$	0.100	mmol cm^{-2}	Estimated from experimental data
Kinetic rate constant in aqueous electrolyte	$k_{CO2,aq}$	1.31	mmol cm^{-2}	Estimated from [41]
IL-based electrolyte bulk pH	pH_{IL}	7.36	—	Estimated from experimental data
Aqueous electrolyte bulk pH	pH_{aq}	6.80	—	Estimated from [41]
Reference exchange current Density in IL-based electrolyte	$i_{o,ref,IL}$	7.77×10^{-3}	A m^{-2}	Estimated from experimental data
Reference exchange current density in aqueous electrolyte	$i_{o,ref,IL}$	4.16×10^{-5}	A m^{-2}	Estimated from [41]
Cathodic transfer coefficient in IL-based electrolyte	$\alpha_{c,IL}$	0.18	—	Estimated from experimental data
Cathodic transfer coefficient in aqueous electrolyte	$\alpha_{c,aq}$	0.14	—	Estimated from [41]
Anodic transfer coefficient	α_a	0.00	—	Estimated from experimental data
Electrolyte density	ρ	1×10^3	Kg m^{-3}	[42]
Electrolyte kinematic viscosity	μ	1×10^{-3}	Pa.s	[42]
Reference temperature	T_{ref}	25	°C	STP
Reference pressure	P_{ref}	1.0	bar	STP

Standard temperature and pressure (STP), ionic liquid (IL), aqueous solution (aq).

The modeling procedure undertaken in this study considered only an electrolytic half-cell, which is a negative electrode, the cathode.

The current collector was implemented by equation (22) on the bottom of the porous cathode, and the applied electric potential (E_{ap}, V vs. RHE) was swept on the surface of the collector:

$$\phi_s = E_{ap}. \tag{22}$$

3. Discussion of results

3.1. Theorical validation

The three-dimensional models created for this simulation study were validated with experimental data from Luo *et al* [41] and our laboratory data collected and measured according to the procedures explained in section 2.1.

To ensure the reliability of the theoretical validation process of the created computational models, the Nelder-Mead smart-search optimization algorithm was used to minimize the squared error between the experimental points and the data resulting from the simulations of the models.

The necessary fitting parameters for the mathematical approximation of the experimental and simulated curves were: 1) the reference exchange current density ($i_{o,ref}$, A m^{-2}), and 2) the cathodic transfer coefficient (α_c), from the Butler–Volmer equation applied to the ECR (equation (17)).

It is also worth mentioning that the experimental data for the models A and C came from a CO_2 electrolysis process in batch operation mode with IL-based electrolyte. In this context, to study the difference in electrochemical performance between batch and continuous flow operation modes in this electrolytic process, the same reference exchange current density ($i_{o,ref}$, A m^{-2}), and cathodic transfer coefficient (α_c) had to be assumed for the validation of the continuous flow model.

Employing the same methodology, the models B and D were validated with experimental data from a continuous flow ECR process in a 0.1 M $KHCO_3$ aqueous electrolyte performed by Luo *et al* [41].

The result of the smart-search optimization process is represented in figure 3. As can be seen, the model that achieved the best fit was A, with a total associated squared error of 0.0007, while model C reached a total associated squared error of 0.7407, which still constitutes a perfectly acceptable fit for the experimental points taken from Luo *et al* [41].

We note that the validation errors reported for the models correspond to the integrated quadratic error over the solution domain. Although Model C shows a higher absolute error value (0.7407) compared to Model A (0.0007), this discrepancy should be interpreted in the context of the model's scale and complexity. All simulations were performed with a relative solver tolerance of 0.001, and the resulting relative errors

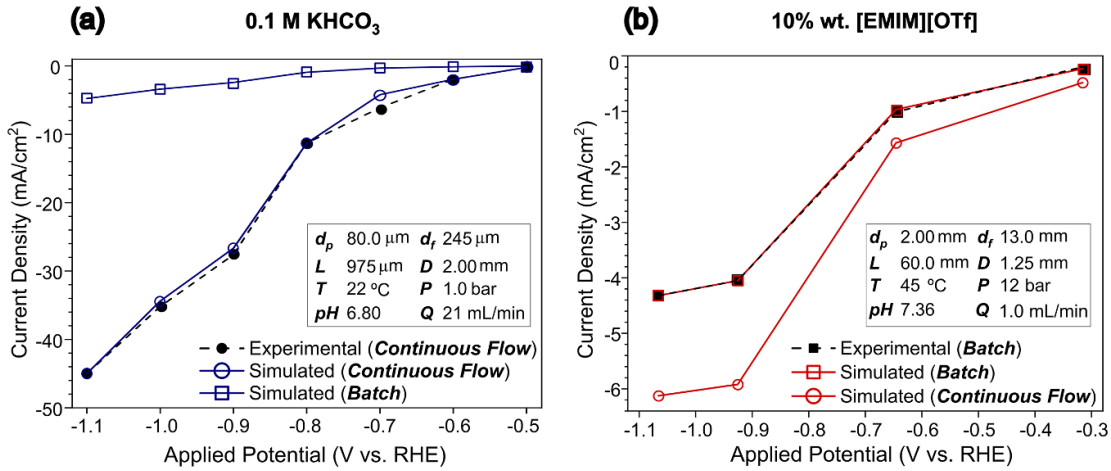

Figure 3. Theoretical validation of the computational models based on the literature data from Luo *et al* [41]. (a) for models batch B and continuous flow D, and experimental data of the present work (b) for models batch A and continuous flow C. Pore diameter (d_p, mm or μm), fiber length (d_f, mm or μm), cathode side (L, mm), cathode thickness (D, mm), electrolyte flow rate (Q, mL min^{-1}), electrolyses pressure (P, bar) and temperature (T, °C).

remain well below this threshold. Therefore, the reported error for Model C is consistent with the expected numerical accuracy, and is considered acceptable within the framework of the solver's convergence criteria.

It can be verified from figure 3 that the error associated with the validation methods was considered negligible for the analyses and improvements discussed in this article. Moreover, it should be noted that all the models demonstrate a good fit with the experimental polarization curves, leading to a high degree of confidence in the mathematical predictions obtained from the simulations of these models. These results also illustrate the influence of the different conductivities of the electrolytes and the use of a porous cathode in generating higher current densities.

3.2. Morphology of the cathode pores

Following the validation of computational models with experimental data from literature [41], and of the present authors, these models were employed to investigate the impact of structural characteristics of the pores constituting the zinc cathode on the current density during ECR and water co-electrolysis (equations (2) and (3)). Specifically, the effects of cathodic porosity (ε, equation (4)), and the number of pores per cathode side (n_L, equation (8)) were examined through parametric sweep studies.

The CO partial current density is the primary performance figure-of-merit of this study. The two operation modes studied, batch (models A and B) and continuous flow (models C and D), show distinct current density production behaviors, indicating that the influence of species concentration on this parameter is largely dependent on the type of electrolyte used (purely aqueous or IL-based electrolyte), and the residence time of the reactants on the porous cathode surface.

3.2.1. Batch operation models

Current density at applied potential of −1.1 V vs. RHE notably increases (in absolute value) with higher cathode porosity (ε) and number of pores per cathode side (n_L), as can be seen in figure 4. Consequently, current density also correlates positively with pore diameter (d_p, μm) and negatively with fiber length (d_f, μm). This observation supports the theoretical understanding that a larger surface area/volume of an electrode leads to higher electrochemical activity and increased current density production.

The main advantage of using aqueous IL-based electrolytes in ECR processes is the large increase in solubility of gaseous CO_2 in the aqueous media, which enhances significantly its availability for reaction at the porous cathode surface of liquid-phase electrolysis.

Indeed, model A, in which electrolyte has a low IL content, performs much better than model B, where a purely aqueous solution with the dissolved $KHCO_3$ salt was used. The CO partial current density at the considered applied potential with the maximum value of porosity (ε) and number of pores per side (n_L) performs about four times higher (more 46.8 mA cm^{-2}) only due to this change in electrolyte. This remarkably illustrates the effect of pressure together with the use of IL in improving system performance.

Several factors can clarify these findings through mechanistic analysis. According to Newman and Tobias [46], higher porosity increases the empty space between catalytic fibers, exposing more surface area to the electrolyte. Additionally, more pores provide more active reaction sites, promoting increased electrochemical

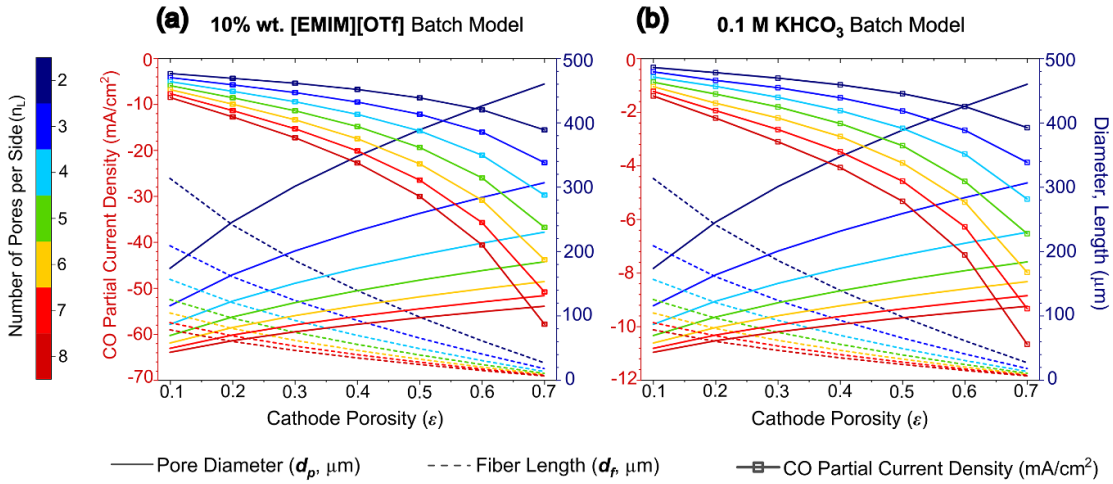

Figure 4. Parametric sweep studies of CO partial current density at applied potential (E_{ap}) of −1.1 V vs. RHE as a function of cathodic porosity (ε) and the number of pores per cathode side (n_L) on the ECR (a) batch model A and (b) batch model B. The temperature and pressure of the electrolyses were $T = 45$ °C and $P = 10$ bar.

activity and faster global reaction kinetics. The double-layer capacitance theory supports this by suggesting improved charge storage and current flow [46].

Mass transport mechanisms also significantly influence current production. Yahya *et al* [47] found that higher porosity reduces mass diffusion resistance for reagents (ions or dissolved gases), enhancing reaction kinetics by shortening their distance to the active sites. Furthermore, fibrous electrodes with multiple pores create parallel diffusion channels, further facilitating mass transport to reactive zones.

Another essential factor is the connectivity between the electrode pores. Bocquet and Charlaix [48] demonstrated that higher porosity enhances ionic and electronic conductivity, thereby increasing current output. Percolation theory models porous networks as electrode surfaces with high connectivity, ensuring more uniform current distribution and avoiding localized overpotentials that could disrupt kinetics [49].

As noted by Lasia [50] and subsequent studies [51], increased porosity and fiber density can reduce activation overpotential, resulting in higher current for the same applied potential, in accordance with the Butler–Volmer equation (equation (17)). A lower Tafel slope with increased cathodic porosity suggests improved charge transport, leading to reduced overpotentials.

Moreover, the conductivity of the electrolyte significantly depends on its saturation with electrochemically dissolved species, as discussed by Song *et al* [52]. Higher porosity allows more electrolyte volume within the cathode, enhancing ion mobility and minimizing ohmic losses. More pores optimize access of ions to active sites, preventing areas with fewer reagents and electrochemical reactions.

High porosity generally indicates a large surface area/volume of an electrode, a finding confirmed in this study. Additionally, a higher number of pores per cathodic side (considering the geometrical assumptions of equations (4) and (5)) results in smaller fiber lengths (d_f, μm) and larger pore diameters (d_p, μm). Maximizing these two geometrical parameters theoretically results in the highest current density at applied potential of −1.1 V vs. RHE.

3.2.2. Continuous flow operation models

Regarding the electrochemical performance of batch (models A and B) vs. continuous operation (models C and D) models, as expected, despite similar geometric configurations, continuous flow model yields much higher current density results for each variable combination presented in figure 5. These results reinforce the reliability of the theoretical validation process despite validation being carried out with experimental results obtained in batch.

Another of the main significant advantages of using aqueous, IL-based electrolytes is the decrease of its inherent kinematic viscosity and density, which allows the enhancement of the flow behavior of the electrolyte inside the electrochemical cell, and through the porous structure of the electrodes [39].

Continuous operation consistently outperforms batch mode, with the performance gap widening as the number of pores per cathodic side increases. For instance, with maximum surface area (higher ε and n_L) at −1.1 V vs. RHE, the CO partial current density achieved is three times higher (more 42.1 mA cm^{-2}) in model C than in model D.

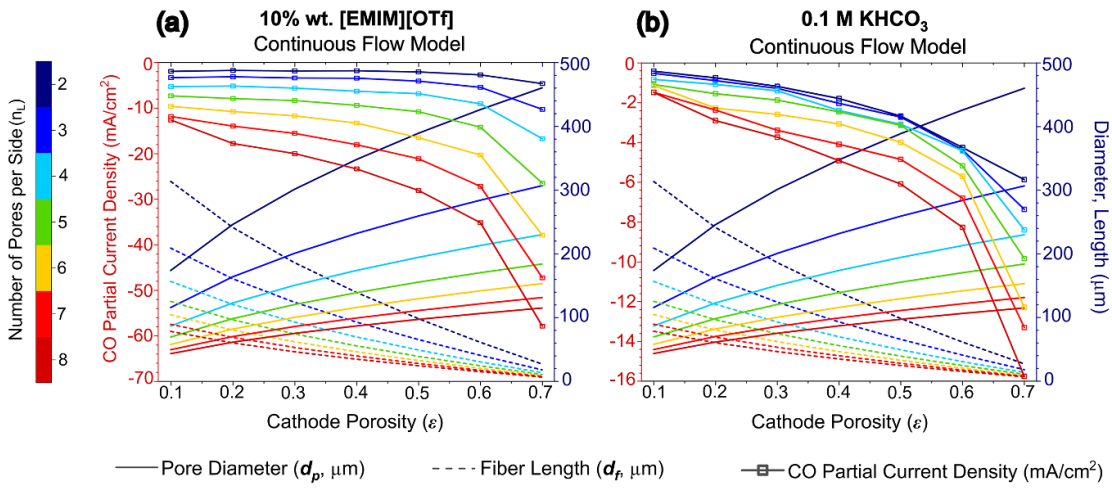

Figure 5. Parametric sweep studies of CO partial current density at applied potential (E_{ap}) of −1.1 V vs. RHE as a function of cathodic porosity (ε) and the number of pores per cathode side (n_L) on the ECR (a) continuous flow model C and (b) continuous flow model D. The temperature and pressure of the electrolyses were T = 45 °C and P = 10 bar. The electrolyte flow rate applied was Q = 2.5 mL min^{-1}.

The best result obtained under the studied operational conditions for all parametric sweep studies shown on section 3.2 was of −57.9 mA cm^{-2}, achieved with $\varepsilon = 0.7$, $n_L = 8$, $d_p = 115$ μm, and $d_f = 7.00$ μm, using model C (continuous flow operation with 10% wt. [EMIM][OTf] aqueous electrolyte).

3.3. Variation of the electrolyte flow rate

The study of the effect of varying the volumetric flow rate (Q, mL min^{-1}) of the different electrolytes, combined with the structural characteristics of the pores of the zinc cathode, was undertaken.

As in section 3.1, the cathode porosity (ε, given by equation (4)) and the number of pores per cathode side (n_L, defined by equation (6)) were the focus of parametric sweep studies. In this section, the operational parameter of the volumetric flow rate of the catholyte (Q, mL min^{-1}) was added to the parameterization of these important structural dimensions of the cathode for improvement of the electrochemical performance of the system.

The results of these parameterized simulations are shown in figure 6, where models C and D are compared with each other, for cathode porosity of 0.7 and number of pores per cathode side of 8. The results for other porosities and number of pores are presented in figure SM.3.

The main observation is that current density increases (in absolute value) with volumetric flow rate of electrolyte (Q, mL min^{-1}) reinforcing the theoretical concept of the predominance of the effect of surface-to-volume area in current density production.

The current density at applied potential of −1.1 V vs. RHE increases with both cathode porosity (ε) and the number of pores per cathode side (n_L), as noted in section 3.2. Additionally, using equations (4)–(6), the electrochemical performance shows a similar relationship with pore diameter (d_p, μm) and fiber length (d_f, μm) as the one observed in the previous section.

These simulations do not align with conclusions from the previous 2D model, which found that lower catholyte flow rates resulted in higher CO partial current density [40]. This conclusion was obtained for various porous cathode configurations using the same volumetric flow rates (Q, mL min^{-1}) as in this study. This difference is a consequence of the significant differences in the porous cathode configurations of both models as already discussed in section 2.2. As before, the use of the IL-based electrolyte enhances significantly CO partial current density.

Nonetheless, the present findings agree with experimental results from previous studies by the authors involving similar electrolytic systems in ECR electrolyzers, in which increasing the electrolyte flow rate (Q, mL min^{-1}) enhanced current density compared to batch operation by increased agitation that improves mass transfer [39, 42].

The best result obtained under the studied operational conditions for the performed parametric sweep studies was of −231 mA cm^{-2}, with $\varepsilon = 0.7$, $n_L = 8$, $d_p = 115$ μm, and $d_f = 7.00$ μm, and $Q = 10$ mL min^{-1}, using model C (use of IL-based electrolyte under continuous flow operation).

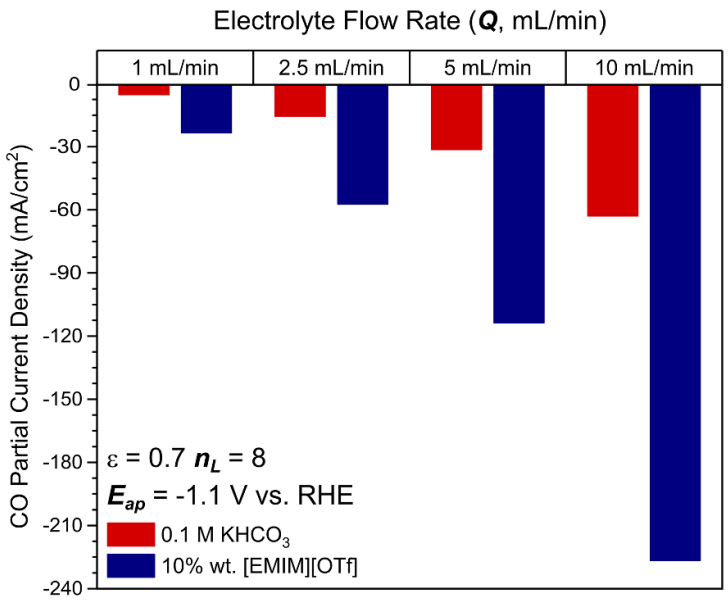

Figure 6. Parametric sweep studies of the CO partial current density at applied potential (E_{ap}) of −1.1 V vs. RHE with porosity (ε) of 0.7 and number of pores per side (n_L) of eight as a function of the flow rate of the electrolyte for the models C (blue bars) and D (red bars). The temperature and pressure of the electrolyses considered were $T = 45$ °C and $P = 10$ bar.

3.4. Effects of pressure and temperature

In this section the effect of temperature and pressure in batch or flow operation modes was investigated. The effect of flow rate for the electrolyte recirculation (Q, mL min^{-1}), cathode porosity (ε), and the number of pores per cathode side (n_L) was also analyzed.

The CO_2 solubility was accounted for in the model via an interpolation function of its experimentally measured concentration in function of pressure and temperature. It was implemented in COMSOL and customized for each kind of studied electrolyte. The CO_2 concentration values were taken from Zakrzewska *et al* [53] for the aqueous IL-based electrolyte system, and by Bisweswar *et al* [54] solubility for the purely aqueous system.

3.4.1. Batch operation models

By increasing operating temperature from 45 ° to 70 °C, the CO partial current density at −1.1 V vs. RHE decreases by a factor of about 0.72 for all combinations of porosity vs. number of pores. This may be due to the decrease in CO_2 solubility in the liquid medium at higher temperatures. CO_2 availability at the porous cathode surface is reduced, decreasing the production rate of the electrochemical reactions. Also, it can be inferred that smaller pore diameter do tend to yield higher current densities for the same values of temperature, pressure and porosity.

In figure 7, the batch models were investigated at pressures of 10, 20 and 40 bar, operating at the temperatures of 45 ° and 70 °C, for porosity of 0.7 and number of pores per side of 8. The results for other porosities and number of pores are depicted in figure SM.4.

Contrasting trends for both electrolytes can be observed. At 45 °C the IL-based electrolyte shows the maximum current density at 10 bar and then the current density decreases with increasing pressure. This may contradict conventional observations, in which high pressure generally enhances CO_2 solubility in aqueous media. However, such behavior can be explained by the favored formation of an IL-CO complex at higher pressures. A discussion of the detailed mechanisms can be found in Messias *et al* [39]. Moreover, since there are several parameters influencing the ECR reaction, such as solubility, or electrolyte nature, this will lead to an optimum value for the operating pressure, which this study proposes to identify. The aqueous electrolyte shows a slight dependance on pressure decreasing from 10 bar to 40 bar. A well-defined temperature-pressure dependence of the current density through different porosities and number of pores per cathode side can also be verified (figure SM.4).

When the temperature increases to 70 °C, current density decreases for pressures of 10 bar and 20 bar and increases at 40 bar pressure for the aqueous electrolyte. In these latter conditions the influence of temperature seems to be dominant in relation to the pressure effect. On the contrary, when the IL-based electrolyte is used, the effect of pressure seems to be dominant, and current density decreases with increasing temperature. This may be due to the decrease in CO_2 solubility in the liquid medium at higher temperatures. CO_2

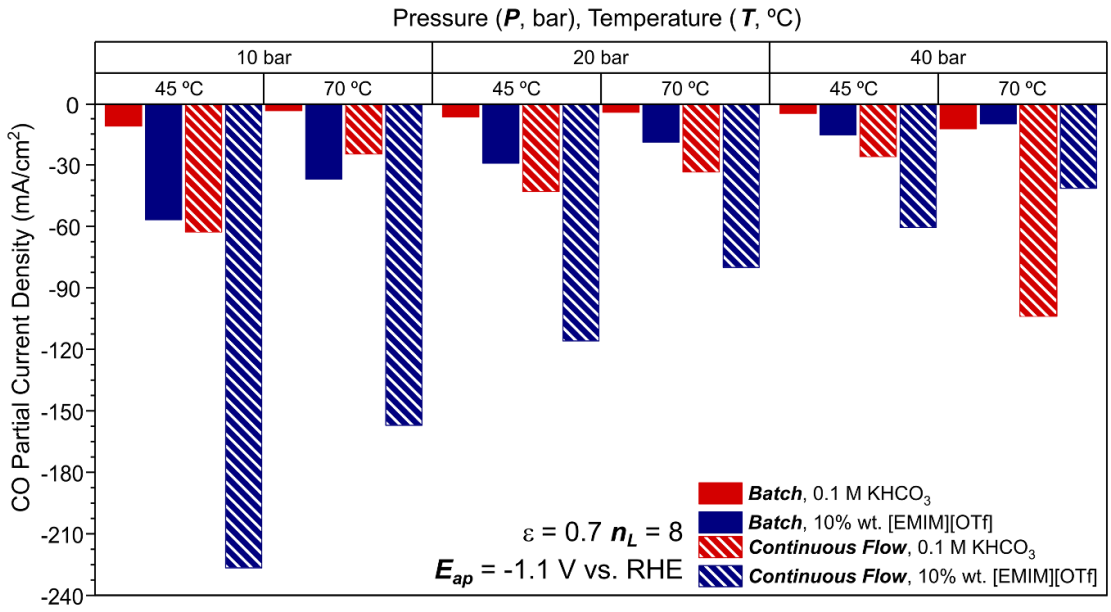

Figure 7. Parametric sweep studies of the deviations of CO partial current density at applied potential (E_{ap}) of −1.1 V vs. RHE with porosity (ε) of 0.7 and number of pores per side (n_L) of 8 as a function of temperature and pressure for the models A (plain blue bars), B (plain red bars), C (blue striped bars), and D (red striped bars). The electrolyte flow rate applied in the continuous flow models C and D was Q = 10 mL min^{-1}.

availability at the porous cathode surface is reduced, decreasing the production rate of the electrochemical reactions. Also, it can be inferred that smaller pore diameters tend to yield higher current densities for the same values of temperature, pressure and porosity, while the opposite happens with pore length.

3.4.2. Continuous flow operation models

Figure 7 also pictures the results for the continuous flow models C and D at an electrolyte flow rate of $Q = 10$ mL min^{-1} at 10, 20 and 40 bar, for 45 and 70 °C, with porosity of 0.7 and number of pores per side of 8. The results for other porosities and number of pores are presented in figure SM.5.

The same trends observed for the batch models can be observed in the flow models but significantly magnified.

The flatness of the curves (figure SM.5) indicates that the mass transport is improved, avoiding the local depletions of the reactants inside the pores. With higher porosity and number of pores, the CO partial current density increases significantly, while the impact of the length of the fibers may be attenuated compared to the batch models. Operation in flow mode helped to reduce some of the mass transport limitations, especially at the lower porosities. The number of pores per cathode side, however, still plays the main role in which higher porosity allows for better access to the active sites of the catalysts, hence increasing current density.

Finally, figures SM.5(e) and (f) combines the models C and D with the highest pressure and temperature scanned ($P = 40$ bar, $T = 70$ °C). In these conditions, the current density is at its peak for the 0.1 M $KHCO_3$ aqueous electrolyte model D, in particular for higher porosities and larger number of pores. A current density of −105 mA cm^{-2} was obtained for $\varepsilon = 0.7$, $n_L = 8$, $d_p = 115$ μm, and $d_f = 7.00$ μm, with $T = 70$ °C, $P = 40$ bar, and $Q = 10$ mL min^{-1}. Indeed, it is possible to take advantage of both the use of high pressure and flow to enhance mass transport, insuring in this way a constant feeding of reactant species into the cathode and, simultaneously, an efficient removal of reaction products. The curves in panels (b), (d), (f) of figure SM.5 are closer together compared to those in panels (a), (c), (e), so there is more similar performance within a range of porosity. Under these enhanced conditions, it appears that pore diameter and fiber length have a relatively minor effect, suggesting mass transport limitations have been largely overcome due to the synergy between flow and high pressure, more notably on the aqueous electrolyte models.

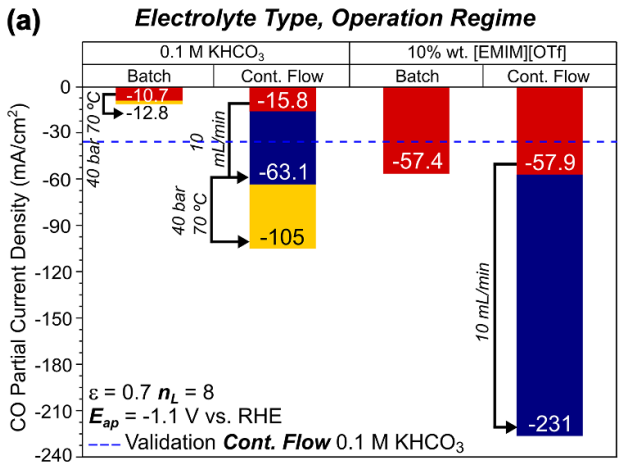

(b)

Optimization Steps	Electrolyte Type	Param.	Val.		Opt.
Morphology of the Cathode Pores	0.1 M $KHCO_3$	d_p (μm)	80.0	→	115
		d_f (μm)	245	→	7.00
	10% wt. [EMIM][OTf]	d_p (μm)	2.00*	→	115
		d_f (μm)	13.0*	→	7.00
Electrolyte Flow Rate	0.1 M $KHCO_3$	Q (mL/min)	21	→	10
	10% wt. [EMIM][OTf]	Q (mL/min)	1.0	→	10
Pressure and Temperature	0.1 M $KHCO_3$	P (bar)	1.0	→	40
		T (°C)	22	→	70
	10% wt. [EMIM][OTf]	P (bar)	12	→	10
		T (°C)	45	→	45

Figure 8. Comparison of the experimental validation data (blue dashed line) to the key findings, concerning the CO partial current density at applied potential (E_{ap}) of −1.1 V vs. RHE, attained by the optimized conditions for ECR at the zinc porous cathodes, according to: (a) the electrolyte type and operation regime; (b) the optimization steps performed, presenting the derived morphological and operating parameters from validated vs. improved cases. Pore diameter (d_p, mm or μm), fiber length (d_f, mm or μm), cathode porosity (ε), number of pores per cathode side (n_L), electrolyte flow rate (Q, mL min^{-1}), electrolyses pressure (P, bar) and temperature (T, °C). * Stands for mm as units for pore diameter and fiber length.

4. Conclusions

This work reports a crucial step forward in the modeling of ECR processes in liquid-phase via porous cathodes, as it is based on a more realistic 3D porous geometry leveraging on a previously developed 2D model. This improvement ensures significantly higher reliability in predicting physical and electrochemical phenomena within the three-dimensional space. The investigation systematically examines structural parameters: porosity, number of pores, dimensions of fiber and pore, operational parameters such as type of electrolyte, flow rate, temperature and pressure.

The main results are summarized in figure 8, depicting the best results attained for each sub-study in this work. During the optimization pathway, the tuning of the electrode 3D morphology was the most significant factor improving the batch process conditions, for both aqueous and IL-based electrolytes. In contrast, under continuous flow operation, the most influential factor for performance improvement was the increase in flow rate, particularly in the IL case. Furthermore, in aqueous electrolytes the performance was also substantially affected by rising temperature and pressure.

The best-performing porous zinc cathode design is shown to produce CO partial current densities of 231 mA cm^{-2} at −1.1 V vs. RHE (25% FE_{CO}, 80% total FE_{syngas}, 35% total EE), at 10 bar, 45 °C, and 10 mL min^{-1}, reaching the threshold for industrial relevant yields. This was observed for the optimized set of parameters attained for the cathode geometry: $\varepsilon = 0.7$, $n = 64$, $d_p = 115$ μm, and $d_f = 7.00$ μm.

Based on the simulation results, the following general remarks can be made for the preparation of high-performance cathodes and process conditions for ECR. The higher the porosity the higher can be the current densities, owing to the larger space available for the diffusional transport of reactants. The pore diameter and fiber length seem to have a stronger influence at ambient pressure and batch operation regime, when the mass transport is more restricted.

Operating at higher pressure significantly increases current density, mainly at low porosity values, more notably under continuous flow using the IL-based electrolyte. The impact of using aqueous IL-based electrolytes clearly demonstrates the potential of achieving relevant industrial current densities.

These results open the way for further improvements, such as exploring the tuneability of ILs with respect to their solubility, viscosity, conductivity, density and co-catalytic properties. The investigation of flow rates and flow patterns through Computational Fluid Dynamics models, to understand the influence of the degree of agitation and residence time on electrochemical performance, is expected to provide clearer perspectives on how mass transfer and reagent consumption may be maximized in the system.

Resorting to advanced preparation methods, such as 3D printing or electrospinning, for the manufacture of porous electrodes, will facilitate the production of structures with controlled geometry, thereby allowing the operational comparison of components with different dimensions to reproduce the computationally predicted geometries, leading to more complete model validation and breakthrough performances.

Data availability statement

All data that support the findings of this study are included within the article (and any supplementary files).

Acknowledgments

This work received funding from FCT (Fundação para a Ciência e Tecnologia, I.P.) under the projects LA/P/0037/2020, UIDP/50025/2020 and UIDB/50025/2020 of the Associate Laboratory Institute of Nanostructures, Nanomodelling and Nanofabrication—i3N, and by the project CO2RED (DOI 10.54499/PTDC/EQU-EPQ/2195/2021). The work was also supported by the project M-ECO2—Industrial cluster for advanced biofuel production, Ref. C644930471-00000041, co-financed by PRR—Recovery and Resilience Plan of the European Union (Next Generation EU).

The authors also acknowledge funding from the European Union via the projects X-STREAM (Horizon EU, ERC CoG, No. 101124803 DOI: https://doi.org/10.3030/101124803) and SolarWay (HORIZON-MSCA-2023-PF-01, No. 101148726 DOI: https://doi.org/10.3030/101148726). Views and opinions expressed are, however, those of the authors only and do not necessarily reflect those of the European Union or the European Research Council. Neither the European Union nor the granting authority can be held responsible for them.

Authors' contributions

Draft of the original manuscript: Fernandes I S, Reis-Machado A S; Conceptualization of work: Reis-Machado A S, Fernandes I S, Mendes M J; Development, implementation of software and validation: Fernandes I S; Experimental work: Messias S; Methodology and investigation: Fernandes I S, Messias S, Reis-Machado A S, Mendes, J M; All authors contributed to review and editing of the manuscript; Supervision and project administration: Mendes M J, Reis-Machado A S; Acquisition of funding for research: Mendes M J, Reis-Machado A S, Martins R.

Conflict of interest

The authors declare that they have no known competing financial interests or personal relationships that could have appeared to influence the work reported in this paper.

ORCID iDs

Sofia Messias 0000-0002-3782-5765
Ana S Reis-Machado 0000-0002-7432-8725

References

[1] Mertens J *et al* 2023 Carbon capture and utilization: more than hiding CO_2 for some time *Joule* **7** 442–9
[2] Reis-Machado A S and Nunes da Ponte M 2018 CO_2 capture and electrochemical conversion *Curr. Opin. Green Sustain. Chem.* **11** 86–90
[3] Chang F, Xiao M, Miao R, Liu Y, Ren M, Jia Z, Han D, Yuan Y, Bai Z and Yang L 2022 Copper-based catalysts for electrochemical carbon dioxide reduction to multicarbon products *Electrochem. Energy Rev.* **5** 4
[4] Messias S, Nunes da Ponte M and Reis-Machado A S 2019 Carbon materials as cathode constituents for electrochemical CO_2 reduction—a review *C* **5** 83
[5] Habibzadeh F, Mardle P, Zhao N, Riley H D, Salvatore D A, Berlinguette C P, Holdcroft S and Shi Z 2023 Ion exchange membranes in electrochemical CO_2 reduction processes *Electrochem. Energy Rev.* **6** 26
[6] Yang Y and Li F 2021 Reactor design for electrochemical CO_2 conversion toward large-scale applications *Curr. Opin. Green Sustain. Chem.* **27** 100419
[7] Vieira F, Sarmento B, Reis-Machado A S, Facão J, Carvalho M J, Mendes M J, Fortunato E and Martins R 2019 Prediction of sunlight-driven CO_2 conversion: producing methane from photovoltaics, and full system design for single-house application *Mater. Today Energy* **14** 100333
[8] Lourenço A C, Reis-Machado A S, Fortunato E, Martins R and Mendes M J 2020 Sunlight-driven CO_2-to-fuel conversion: exploring thermal and electrical coupling between photovoltaic and electrochemical systems for optimum solar-methane production *Mater. Today Energy* **17** 100425
[9] Delacourt C, Ridgway P L, Kerr J B and Newman J 2007 Design of an electrochemical cell making syngas ($CO + H_2$) from CO_2 and H_2O reduction at room temperature *J. Electrochem. Soc.* **155** B42
[10] Georgopoulou C, Jain S, Agarwal A, Rode E, Dimopoulos G, Sridhar N and Kakalis N 2016 On the modelling of multidisciplinary electrochemical systems with application on the electrochemical conversion of CO_2 to formate/formic acid *Comput. Chem. Eng.* **93** 160–70
[11] Dinh C-T *et al* 2018 CO_2 electroreduction to ethylene via hydroxide-mediated copper catalysis at an abrupt interface *Science* **360** 783–7

[12] Tan Y C, Lee K B, Song H and Oh J 2020 Modulating local CO_2 concentration as a general strategy for enhancing C−C coupling in CO_2 electroreduction *Joule* **4** 1104–20
[13] Weng L-C, Bell A T and Weber A Z 2019 Towards membrane-electrode assembly systems for CO_2 reduction: a modeling study *Energy Environ. Sci.* **12** 1950–68
[14] Brée L C, Wessling M and Mitsos A 2020 Modular modeling of electrochemical reactors: comparison of CO_2-electolyzers *Comput. Chem. Eng.* **139** 106890
[15] El-Shafie O A, El-Maghraby R M, Albo J, Fateen S-E K and Abdelghany A 2020 Modeling and numerical investigation of the performance of gas diffusion electrodes for the electrochemical reduction of carbon dioxide to methanol *Ind. Eng. Chem. Res.* **59** 20929–42
[16] Wheeler D G, Mowbray B A W, Reyes A, Habibzadeh F, He J and Berlinguette C P 2020 Quantification of water transport in a CO_2 electrolyzer *Energy Environ. Sci.* **13** 5126–34
[17] Kas R, Star A G, Yang K, Van Cleve T, Neyerlin K C and Smith W A 2021 Along the channel gradients impact on the spatioactivity of gas diffusion electrodes at high conversions during CO_2 electroreduction *ACS Sustain. Chem. Eng.* **9** 1286–96
[18] Blake J W, Padding J T and Haverkort J W 2021 Analytical modelling of CO_2 reduction in gas-diffusion electrode catalyst layers *Electrochim. Acta* **393** 138987
[19] Heßelmann M, Bräsel B C, Keller R G and Wessling M 2023 Simulation-based guidance for improving CO_2 reduction on silver gas diffusion electrodes *Electrochem. Sci. Adv.* **3** 2100160
[20] Weekes D M, Salvatore D A, Reyes A, Huang A and Berlinguette C P 2018 Electrolytic CO_2 reduction in a flow cell *Acc. Chem. Res.* **51** 910–8
[21] Chen Y, Lewis N S and Xiang C 2020 Modeling the performance of a flow-through gas diffusion electrode for electrochemical reduction of CO or CO_2 *J. Electrochem. Soc.* **167** 114503
[22] Löffelholz M, Osiewacz J, Lüken A, Perrey K, Bulan A and Turek T 2022 Modeling electrochemical CO_2 reduction at silver gas diffusion electrodes using a TFFA approach *Chem. Eng. J.* **435** 134920
[23] Agarwal V G and Haussener S 2024 Quantifying mass transport limitations in a microfluidic CO_2 electrolyzer with a gas diffusion cathode *Commun. Chem.* **7** 1–15
[24] Hori Y, Kikuchi K, Murata A and Suzuki S 1986 Production of methane and ethylene in electrochemical reduction of carbon dioxide at copper electrode in aqueous hydrogencarbonate solution *Chem. Lett.* **15** 897–8
[25] Hori Y, Murata A, Takahashi R and Suzuki S 1988 Enhanced formation of ethylene and alcohols at ambient temperature and pressure in electrochemical reduction of carbon dioxide at a copper electrode *J. Chem. Soc. Chem. Commun.* **1** 17–19
[26] Hori Y, Takahashi R, Yoshinami Y and Murata A 1997 Electrochemical reduction of CO at a copper electrode *J. Phys. Chem. B* **101** 7075–81
[27] Hori Y, Takahashi I, Koga O and Hoshi N 2003 Electrochemical reduction of carbon dioxide at various series of copper single crystal electrodes *J. Mol. Catal. Chem.* **199** 39–47
[28] Kas R, Hummadi K K, Kortlever R, de Wit P, Milbrat A, Luiten-Olieman M W J, Benes N E, Koper M T M and Mul G 2016 Three-dimensional porous hollow fibre copper electrodes for efficient and high-rate electrochemical carbon dioxide reduction *Nat. Commun.* **7** 10748
[29] Lv J-J, Jouny M, Luc W, Zhu W, Zhu J-J and Jiao F 2018 A highly porous copper electrocatalyst for carbon dioxide reduction *Adv. Mater.* **30** 1803111
[30] Chen L, Li F, Zhang Y, Bentley C L, Horne M, Bond A M and Zhang J 2017 Electrochemical reduction of carbon dioxide in a monoethanolamine capture medium *ChemSusChem* **10** 4109–18
[31] Kim Y, Lees E W and Berlinguette C P 2022 Permeability matters when reducing CO_2 in an electrochemical flow cell *ACS Energy Lett.* **7** 2382–7
[32] Yang H B *et al* 2018 Atomically dispersed Ni(i) as the active site for electrochemical CO_2 reduction *Nat. Energy* **3** 140–7
[33] Asadi M *et al* 2014 Robust carbon dioxide reduction on molybdenum disulphide edges *Nat. Commun.* **5** 4470
[34] Li M, Garg S, Chang X, Ge L, Li L, Konarova M, Rufford T E, Rudolph V and Wang G 2020 Toward excellence of transition metal-based catalysts for CO_2 electrochemical reduction: an overview of strategies and rationales *Small Methods* **4** 2000033
[35] Lin J, Yan S, Zhang C, Hu Q and Cheng Z 2022 Electroreduction of CO_2 toward high current density *Processes* **10** 826
[36] Lucile F, Cézac P, Contamine F, Serin J-P, Houssin D and Arpentinier P 2012 Solubility of carbon dioxide in water and aqueous solution containing sodium hydroxide at temperatures from (293.15–393.15) K and pressure up to 5 MPa: experimental measurements *J. Chem. Eng. Data* **57** 784–9
[37] Singh M R, Clark E L and Bell A T 2015 Effects of electrolyte, catalyst, and membrane composition and operating conditions on the performance of solar-driven electrochemical reduction of carbon dioxide *Phys. Chem. Chem. Phys.* **17** 18924–36
[38] Rosen B A, Salehi-Khojin A, Thorson M R, Zhu W, Whipple D T, Kenis P J A and Masel R I 2011 Ionic liquid-mediated selective conversion of CO_2 to CO at low overpotentials *Science* **334** 643–4
[39] Messias S, Paz V, Cruz H, Rangel C M, Branco L C and Reis-Machado A S 2022 Imidazolium and picolinium-based electrolytes for electrochemical reduction of CO_2 at high pressure *Energy Adv.* **1** 277–86
[40] Fernandes I S, Antunes D, Martins R, Mendes M J and Reis-Machado A S 2024 Solar fuels design: porous cathodes modeling for electrochemical carbon dioxide reduction in aqueous electrolytes *Heliyon* **10** e26442
[41] Luo W, Zhang J, Li M and Züttel A 2019 Boosting CO production in electrocatalytic CO_2 reduction on highly porous Zn catalysts *ACS Catal.* **9** 3783–91
[42] Messias S, Sousa M M, da Ponte M N, Rangel C M, Pardal T and Machado A S R 2019 Electrochemical production of syngas from CO_2 at pressures up to 30 bar in electrolytes containing ionic liquid *React. Chem. Eng.* **4** 1982–90
[43] Nield D A and Bejan A (eds) 2006 Mass transfer in a porous medium: multicomponent and multiphase flows *Convection Porous Media* (Springer) pp 39–56
[44] Desalvo A, Gondi P, Levi F A and Zignani F 1964 Electrical conductivity of high-purity zinc *Nuovo Cimento* **31** 904–13
[45] Nitopi S *et al* 2019 Progress and perspectives of electrochemical CO_2 reduction on copper in aqueous electrolyte *Chem. Rev.* **119** 7610–72
[46] Newman J S and Tobias C W 1962 Theoretical analysis of current distribution in porous electrodes *J. Electrochem. Soc.* **109** 1183
[47] Yahya A, Naji H and Dhahri H 2023 A lattice Boltzmann analysis of the performance and mass transport of a solid oxide fuel cell with a partially obstructed anode flow channel *Fuel* **334** 126537
[48] Bocquet L and Charlaix E 2010 Nanofluidics, from bulk to interfaces *Chem. Soc. Rev.* **39** 1073–95
[49] Urban A 2024 Modeling ionic transport and disorder in crystalline electrodes using percolation theory *Computational Design Battery Materials* ed D A H Hanaor (Springer) pp 169–85

[50] Lasia A 2014 *Electrochemical Impedance Spectroscopy and Its Applications* (Springer) (https://doi.org/10.1007/978-1-4614-8933-7)
[51] Bhargava S S, Proietto F, Azmoodeh D, Cofell E R, Henckel D A, Verma S, Brooks C J, Gewirth A A and Kenis P J A 2020 System design rules for intensifying the electrochemical reduction of CO_2 to CO on Ag nanoparticles *ChemElectroChem* **7** 2001–11
[52] Song K, Li W, Chen Z, Wu X, Zhou Q, Snyder K and Zhang L 2021 An effective approach to improve electrochemical performance of thick electrodes *Ionics* **27** 1261–70
[53] Zakrzewska M E and Nunes da Ponte M 2018 Influence of water on the carbon dioxide solubility in [OTf]- and [eFAP]-based ionic liquids *J. Chem. Eng. Data* **63** 907–12
[54] Bisweswar G, Al-Hamairi A and Jin S 2020 Carbonated water injection: an efficient EOR approach. A review of fundamentals and prospects *J. Pet. Explor. Prod. Technol.* **10** 673–85